

Interacting holes in gated WSe₂ quantum dots

Daniel Miravet,¹ Abdulmenaf Altıntaş,¹ Alina Wania Rodrigues,¹
Maciej Bieniek,^{2,3} Marek Korkusinski,^{1,4} and Paweł Hawrylak¹

¹*Department of Physics, University of Ottawa, Ottawa, Ontario, Canada K1N 6N5*

²*Institut für Theoretische Physik und Astrophysik,
Universität Würzburg, 97074 Würzburg, Germany*

³*Institute of Theoretical Physics, Wrocław University of Science and Technology,
Wybrzeże Wyspiańskiego 27, 50-370 Wrocław, Poland*

⁴*Security and Disruptive Technologies, National Research Council, Ottawa, K1A0R6, Canada*

(Dated: August 11, 2023)

We develop here a theory of the electronic properties of a finite number of valence holes in gated WSe₂ quantum dots, considering the influence of spin, valley, electronic orbitals, and many-body interactions. The single-particle wave functions are constructed by combining the spin-up and down states of the highest valence bulk bands employing a multi-million atom ab-initio based tight-binding model solved in the wave-vector space, allowing to study up to 100 nm radius quantum dots atomistically. The effects of the many-body interactions are determined using the configuration interaction (CI) technique, applied up to $N = 6$ holes occupying up to 6 electronic shells with 42 orbitals. Our results show that $N=2$ holes are in valley and spin anti-ferromagnetic ground state, independent of the interaction strength and the quantum dot size. However, we predict that higher number of holes can undergo a transition to spontaneously broken symmetry valley and spin polarized ferromagnetic phases, highlighting the interplay between the many-body effects and the quantum dot lateral size and confining potential depth.

I. INTRODUCTION

Single layers of transition metal dichalcogenides (TMDCs) have emerged as an interesting class of materials with rich spectrum of electronic, optical and magnetic properties owing to the interplay between strong electron-electron interactions and their low-dimensional nature. The fabrication of TMDCs at the few atomic layer scale has unlocked new directions in the low-dimensional physics [1–12]. In contrast with monolayer graphene, TMDCs exhibit a band gap, which makes them attractive for optoelectronic applications [12–14].

TMDCs unit cell consists of a metal atom (Mo or W) and a chalcogenide dimer (S₂, Se₂ or Te₂), with the electronic and optical properties primarily governed by the d orbitals of the metal atoms [15–17]. The presence of strongly localized d orbitals of the transition metal atoms, coupled with the reduced screening in two dimensions, leads to pronounced correlation effects, which in turn give rise to insulating behavior and the formation of excitons with large binding energies [18–21].

Additionally, the spin-orbit coupling present in TMDCs plays an important role, leading to the realization of unique spin-dependent phenomena. Due to the conservation of time-reversal symmetry, valleys K and -K exhibit opposite spin splittings, resulting in a spin-valley locking effect. In particular, WSe₂ stands out due to its large spin-orbit splitting of approximately 500 meV in the valence band, distinguishing it from other TMDC compounds [22, 23]. Moreover, it is worth noting that while the bottom of the conduction band in valleys K and -K is predominantly composed of $m_d = 0$ orbitals, the top of the valence band in valleys K and -K is primarily composed of $m_d = -2$ and $m_d = 2$ orbitals, respectively [16].

This orbital asymmetry between the valleys can give rise to novel features in hole systems, leading to intriguing phenomena and potential applications in spintronics and quantum information processing [15].

The progress in graphene and TMDC materials led to the creation of lateral quantum dots (QDs) by the application of an electrostatic confinement [24–35]. Application of lateral metallic gates results in the lateral electrostatic confinement of electrons or holes, resulting in the creation of atomic-like states [6, 15, 16, 32–34, 36–43].

In this study we develop a theory of the electronic properties of finite number of valence holes in gated WSe₂ quantum dots, considering the influence of spin, valley, electronic orbitals, and many-body interactions [6, 42, 44]. The shell spacing ω of the atomic-like quantum dot levels strongly depends on the lateral size and depth of confining potential embedded in WSe₂ computational box size. Here, we investigate computational boxes containing millions of atomic orbitals, allowing for a comprehensive exploration of the effects of strong interactions on the ground and excited states of valence holes confined by lateral potentials to a quantum dot of definite lateral size and potential depth.

The paper is structured as follows. In Section II, we provide a comprehensive description of the single-particle states in the gated WSe₂ quantum dot, along with an overview of the formulation of the many-body problem. The results of the many-body low-energy spectrum are presented in Section III. Specifically, in Subsection III A, we analyze the case of $N = 2$ and $N = 4$ holes, while in Subsection III B, we focus on the scenario involving $N = 6$ holes. The paper concludes with a summary and key findings in Section IV.

II. MODEL

A. Single Particle Properties

The single particle Hamiltonian describing a hole in a single layer of WSe₂ QD can be expressed as the sum of the bulk Hamiltonian H_b and the confining potential V_{QD} [15]. In this work, we model the potential $V_{QD}(\vec{r})$ as a Gaussian gate potential given by $V_{QD}(\vec{r}) = V_0 \exp(-r^2/R_{QD}^2)$, where V_0 is the potential depth and R_{QD} corresponds to the QD radius, see Fig. 2(a). Here we will use a typical potential depth $V_0 = 300$ meV and vary the quantum dot radius R_{QD} . The wavefunction $|\Phi^s\rangle$ of the hole in the QD, associated with the state s can be determined by solving the Schrödinger equation:

$$(H_b + V_{QD}(\vec{r})) |\Phi^s\rangle = E^s |\Phi^s\rangle. \quad (1)$$

To describe the valence band (VB) wavefunction of our quantum dot, we adopt a method similar to that developed in Ref. [15] for electrons in the conduction band. In this approach, we construct the VB wavefunction at each wave-vector k as a linear combination of simple Bloch functions on the tungsten and selenium atoms sublattices. Specifically, we consider six such Bloch functions enumerated by the index l ($l = 1, \dots, 6$):

$$|\phi_{k\sigma}^{\text{VB}}\rangle = \sum_{l=1}^6 A_{k\sigma,l}^{\text{VB}} |\phi_{k,l}\rangle \otimes |\chi_\sigma\rangle, \quad (2)$$

where $|\chi_\sigma\rangle$ represents the spinor part of the wavefunction and

$$|\phi_{k,l}\rangle = \frac{1}{\sqrt{N_{\text{UC}}}} \sum_{\vec{R}_l=1}^{N_{\text{UC}}} e^{i\vec{k}\vec{R}_l} \varphi_l(\vec{r} - \vec{R}_l), \quad (3)$$

are simple Bloch functions built with orbitals φ_l even with respect to the metal plane. N_{UC} is the number of unit cells and R_l defines the position of orbitals in the computational box. By diagonalizing the 6×6 bulk Hamiltonian we obtain the even bulk energy bands $E_{k\sigma}^{\text{VB}}$ and wavefunctions $A_{k\sigma,l}^{\text{VB}}$.

Figure 1 shows the energy $E_{k\sigma}^{\text{VB}}$ of the hole in the highest even valence band (VB) and provides a map of the valence band energies across the rhombus in the k -space where the computations are conducted, encompassing the $+K$ and $-K$ valley maxima. It is important to note that the spin splitting Δ_{SOC} is opposite in these valleys, with a magnitude of approximately 470 meV [22].

The QD wavefunction $|\Phi^s\rangle$ can be expanded in terms of the highest even energy valence band states given by Eq. 2:

$$|\Phi^s\rangle = \sum_{\vec{k}} \sum_{\sigma} B_{\vec{k}\sigma}^{\text{s,VB}} |\phi_{\vec{k}\sigma}^{\text{VB}}\rangle. \quad (4)$$

The Schrödinger equation can now be expressed as an

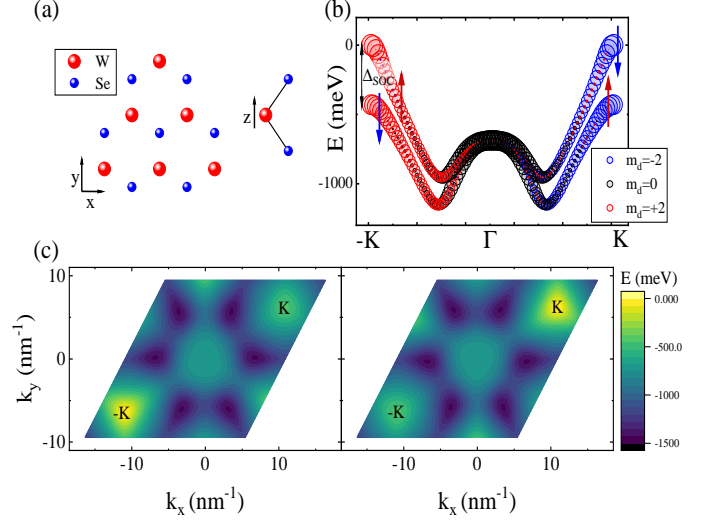


FIG. 1. (Color online) (a) Schematic representation of a monolayer WSe₂. The red (blue) dots represent W (Se) atoms. (b) Highest energy valence band as a function of wavevector k over the path $-K \rightarrow \Gamma \rightarrow +K$. The states in the $+K$ valley are composed mainly of $m_d = -2$ orbitals, while states in the $-K$ valley are composed mainly of $m_d = +2$ orbitals. (c) Energy levels of the highest valence band in the bulk WSe₂ at different allowed values of k points, shown from left to right for spin-up and spin-down states. The $+K$ and $-K$ points represent the global valley maxima of the valence band.

integral equation for the coefficients $B_{\vec{k}\sigma}^{\text{s,VB}}$

$$E_{q\sigma}^{\text{VB}} B_{q\sigma}^{\text{s,VB}} + \sum_{\vec{k}\sigma'} V_{q,k} A_{q\sigma,k\sigma'} B_{k\sigma'}^{\text{s,VB}} = E^s B_{q\sigma}^{\text{s,VB}}. \quad (5)$$

Here, the QD confining potential in the wavevector space is represented as a product of the lateral electrostatic confinement potential $V_{q,k}$ and the band contribution $A_{q\sigma,k\sigma'}$, with

$$V_{q,k} = V_0 \frac{S}{4\pi} R_{QD}^2 \exp\left(-\frac{(k-q)^2}{4} R_{QD}^2\right), \quad (6)$$

where $V_{q,k}$ is the Fourier transform of the confining potential. S corresponds to the reciprocal lattice unit cell area. The band structure contribution to the scattering potential $A_{q\sigma,k\sigma'}$ is given by

$$A_{q\sigma,k\sigma'} = \sum_l (A_{q\sigma,l}^{\text{VB}})^\dagger (A_{k\sigma',l}^{\text{VB}}). \quad (7)$$

To facilitate numerical calculations, we use a computational box that accommodates a maximum of $N_1 \times N_2 = 1011 \times 1011$ unit cells, the specific size depending on the QD defined by metallic gates under consideration. This corresponds to a total of $3 \cdot N_1 \times N_2 = 3,066,363$ atoms. To handle such a large number of atoms, periodic boundary conditions are imposed on the computational domain, creating a discrete set of k points in the reciprocal space.

Since we focus on the highest valence band states, we apply a cutoff to the k points near K and $-K$ by selecting values of k that satisfy the condition $|k \pm K| < \eta|K|$. This approach helps us to focus on the relevant region of the reciprocal space. To ensure the convergence of the QD single-particle states, we set a fixed value of $\eta = 0.1$. By using this modified set of k points, Eq. 5 becomes computationally manageable, enabling us to perform our calculations effectively.

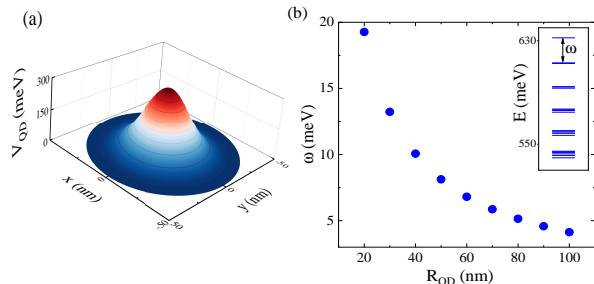


FIG. 2. (Color online) Hole confining potential for a gate potential depth of $V_0 = 300$ meV and a QD radius of $R_{QD} = 20$ nm. The potential creates a localized region where holes are confined. (b) Dependence of the inter-shell spacing ω on the QD radius. (inset) QD spectrum for $R_{QD} = 20$ nm, showing the energy levels of the confined holes. The applied negative gate potential leads to the formation of harmonic oscillator-like shell structures in the states of the QD.

We obtain the QD energy levels and wavefunctions by solving Eq. 5. Figure 2 (b) shows the energy difference between the two highest confined shells. The inset in Figure 2 (b) shows the energy levels of a hole confined within a QD of radius 20 nm. It is evident from the plot that the energy levels exhibit a distinctive grouping into shells. Notably, the highest energy shell comprises of two states, corresponding to the spin-down and spin-up configurations, situated in the $+K$ and $-K$ valleys, respectively.

Despite the cylindrical symmetry of the confining potential, we observe an intrashell splitting phenomenon. This intriguing observation has been previously reported [16] and can be compared to self-assembled quantum dots (QDs) subjected to an applied magnetic field [45]. The observed intrashell splitting can be attributed to the presence of Berry curvature, which can be understood as an effective magnetic field that acts on the angular momentum states in opposite directions in the K and $-K$ valleys [46, 47].

B. Many-body Interactions

We now consider the problem where N holes occupy the valence single-particle states within the QD. In this case, the interacting Hamiltonian for holes can be written

as

$$H = - \sum_p E^p c_p^\dagger c_p + \frac{1}{2} \sum_{p,q,r,s} \langle pq | V | rs \rangle c_p^\dagger c_q^\dagger c_r c_s. \quad (8)$$

Here, E^p represents the energies of the QD single-particle states, which are obtained by solving Eq. 5. The operator c_p^\dagger (c_p) creates (annihilates) a hole in the QD state p . The Coulomb matrix elements, denoted as $\langle pq | V | rs \rangle$, are expressed in terms of the QD single-particle orbitals as

$$\langle pq | V | rs \rangle = \int d\vec{r}_1 \int d\vec{r}_2 \Phi^p(\vec{r}_1)^* \Phi^q(\vec{r}_2)^* V(\vec{r}_2 - \vec{r}_1) \times \Phi^r(\vec{r}_2) \Phi^s(\vec{r}_1), \quad (9)$$

where $\Phi^p(\vec{r}) = \langle \vec{r} | \Phi^p \rangle$. The interaction V is given by the Coulomb potential with Keldysh screening [42, 48]

$$V(\vec{r}_2 - \vec{r}_1) = \frac{e^2}{4\pi\epsilon_0\epsilon} \frac{1}{(2\pi)^2} \int \frac{2\pi}{|k|} \frac{1}{1 + 2\pi\alpha|k|} e^{-|z_2 - z_1||\vec{k}|} \times e^{i\vec{k}\cdot(\vec{r}_2 - \vec{r}_1)} d^2\vec{k}, \quad (10)$$

where $\vec{r} = (\vec{\rho}, z)$, $\alpha = 2.2$ is the 2D polarizability and ϵ is the relative dielectric constant. We will use $\epsilon = 6.0$ in this work.

To diagonalize the many-body Hamiltonian represented by Eq. 8 we use the configuration-interaction (CI) approach. This involves generating all possible configurations of the N holes occupying a specific number of single-particle orbitals, constructing the many-body Hamiltonian matrix in the space of configurations, diagonalizing this matrix, and obtaining the energy spectrum and many-body eigenstates.

III. NUMERICAL EXACT DIAGONALIZATION AND DISCUSSION OF RESULTS

We consider QDs of diameters up to 100 nm and up to 42 single-particle valence band states (6 shells), which we then fill with up to 6 holes. Due to the large spin-orbit coupling in the valence band of WSe_2 , the complete shell of single-particle levels splits into sub-shells. This spin splitting gives rise to a spin-valley locking effect, whereby the QD states near the top of the valence band have spin down and up in the $+K$ and $-K$ valleys, respectively. Hence, it is safe to concentrate only on the highest subshells that are well isolated from the subshells pushed deep into the valence band, as shown in Figure 1.

Shell spacing of the energy levels is inversely proportional to the QD's radius, which can be seen in Figure 2 (b). On the other hand, the strength of the Coulomb interactions is directly proportional to the square root of the shell spacing ω which can be seen in Figure 3. Here, $V_{i,j}^d$ ($V_{i,j}^x$) refers to the direct (exchange) interaction between the levels i and j . Furthermore, the effect of the interactions is increasing with the QD radius as shown in Figure 3.

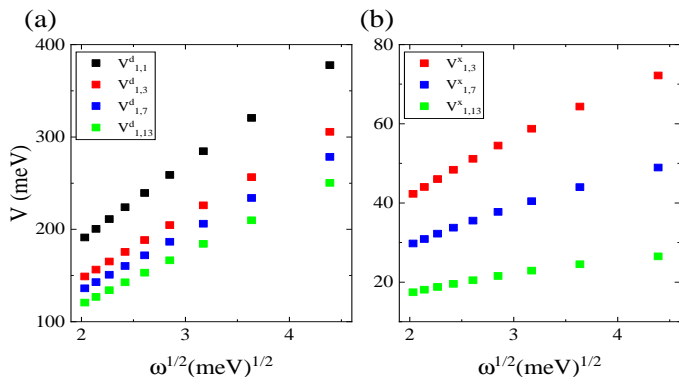


FIG. 3. (Color online) Coulomb matrix elements for single particle QD states as a function of shell energy spacing $\sqrt{\omega}$. (a) Direct Coulomb matrix elements and (b) exchange Coulomb matrix elements with Keldysh screening. The notation $V_{i,j}^d$ ($V_{i,j}^x$) denotes the interaction between the levels i and j , indicating the strength of the direct (exchange) interaction between these levels.

A. $N = 2, 4$ holes

Figure 4 (a) shows the low energy spectrum for a QD with $R_{QD} = 20$ nm. Ground state reference energy is chosen at $E = 0$. The ground state is an unpolarized and fully intervalley antiferromagnetic state.

The stability of the ground state compared with other phases is partly determined by the energy difference between the ground state and the first excited state ΔE_{X-GS} . Figure 4 (c) shows the dependence of the singlet-triplet gap on the QD size. In this case, by increasing the radius (increasing interaction effects) the gap decreases.

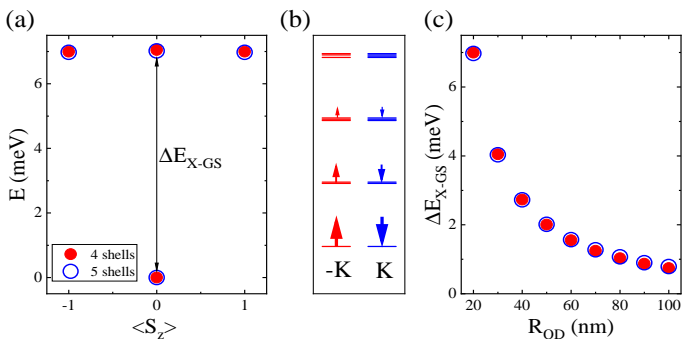


FIG. 4. (Color online) (a) Low energy spectrum for $N = 2$ holes in QD with $R_{QD} = 20$ nm QD. The ground state is a singlet, followed by triplet excited states. (b) Schematic representation of the ground-state occupation of single-particle QD orbitals. (c) Dependence of the singlet-triplet gap on the QD size, showing how energy separation between singlet and triplet states varies with the QD radius.

For $N = 2$, the non-interacting ground state has the first shell completely filled. However, the Coulomb interaction changes this picture notably. Figure 4 (b)

schematically shows the occupation of the single particle QD states in the many body ground state. The holes tend to occupy mainly the first shell like in the non-interacting ground state, although there is some finite occupation in the third shell induced by the Coulomb repulsion. In this case, the result for 4 and 5 shell shells are equivalent for all the QD sizes considered.

For $N = 4$ the non-interacting ground state has the second shell half-filled. The low energy spectrum for $N = 4$ interacting holes is shown in Figure 5. Here, the excitation gap ΔE_{X-GS} is smaller than for $N = 2$ holes, the ground state is a triplet, with two states spin and valley polarized, and one unpolarized. Figure 5 (d) shows the dependence of the triplet-singlet gap on the QD size. The difference in the gap between the result for 4 and 5 shells is almost constant over the range of QD radius considered.

Figures 5 (b) and (c) provide a schematic illustration of the ground-state occupation of single-particle QD orbitals for both unpolarized ($S_z = 0$) and polarized ($S_z = 1$) states, respectively. In the unpolarized case, the occupation pattern is similar to that of non-interacting systems, except for some higher energy orbitals being occupied due to the interactions. However, in the polarized state, the occupation profile deviates more significantly from the non-interacting case. Specifically, the first shell is partially spin-polarized, while the second shell is fully spin-polarized. This finding highlights the strong impact of the electron-electron interactions on the ground-state properties of QDs, especially in the polarized regime.

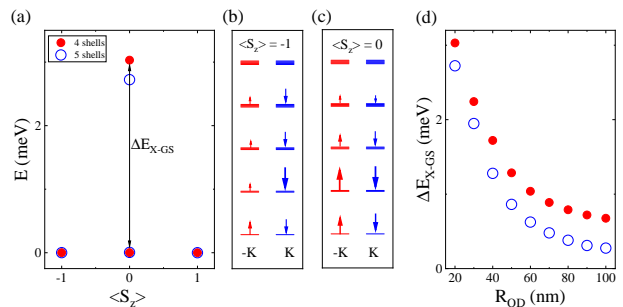


FIG. 5. (Color online) (a) Low energy spectrum for $N = 4$ holes in QD with $R_{QD} = 20$ nm QD. The ground state is a triplet, followed by a singlet excited state. (b), (c) shows the schematic representation of the ground-state occupation of single-particle QD orbitals. (d) Dependence of the triplet-singlet gap with the QD size.

B. $N = 6$ holes states

Figure 6 (a) depicts the low-energy spectrum for a QD with $R_{QD} = 20$ nm, considering the presence of $N = 6$ holes. The corresponding spectrum for $R_{QD} = 50$ nm is shown in Fig. 6 (c). The behavior observed in the spectrum is complex and depends on the number of shells

considered in the CI calculations. The number of shells is controlled by potential depth V_0 .

For calculations involving 4 shells, the ground state is consistently a singlet across different values of R_{QD} . However, the excitation gap decreases as the QD radius increases. In the case of 5 shells included in the basis, the ground state remains a singlet for $R_{QD} < 30$ nm, while for $R_{QD} > 30$ nm the interaction effects become more significant, leading to a ground state with a quintuple character. To further explore this phenomenon, an additional shell is included in the calculations for $N = 6$ holes. Surprisingly, the resulting low-energy spectrum exhibits more similarities to the result obtained using only 4 shells rather than those obtained with 5 shells. Similar behavior has been observed in previous studies of parabolic QDs [49].

This behavior can be attributed to the repulsion between holes, particularly the direct term of the Coulomb interaction. As depicted in Figures 6 (b) and (d), by increasing R_{QD} the particles tend to spread into more shells, thereby minimizing the Coulomb repulsion. However, this also results in an increase in the kinetic energy. The ratio between the Coulomb interaction and the kinetic inter-shell gap (ω) increases with the QD radius (see Figure 3). This implies that the kinetic energy gain associated with occupying higher energy shells is only compensated for larger QD sizes.

To obtain a more accurate determination of the ground state for $N = 6$ holes, irrespective of the depth of confining potential, it is necessary to include additional shells in our calculations. However, we have already reached the limits of our CI capabilities in terms of computational resources. One potential approach to address this challenge is to employ a ground state calculation using a Matrix Product State (MPS) - Density Matrix Renormalization Group (DMRG) scheme [50, 51]. This method while variational in nature has proven successful in studying many-body systems and can potentially extend our results to a larger number of shells. However, the presence of long-range interactions, as observed in Figure 3, may complicate the application of the MPS-DMRG scheme for this particular system. In future work, we plan to investigate different many-body states by extending the number of shells and exploring the feasibility and benefits of the MPS-DMRG approaches to obtain more comprehensive insights into the system's behavior. However, we also point to the fact that the number of shells is controlled by the depth V_0 of the confining potential and hence different ground states for different depths predicted in this study are to be expected.

IV. CONCLUSIONS

In this study, we presented an investigation of the electronic properties of finite numbers of valence holes in gated WSe₂ quantum dots, considering the influence of spin, valley, orbital, and many-body interactions on the low-energy spectrum. By employing a multi-million atom tight-binding model solved in the wave-vector space, we have obtained single-particle states characterized by the harmonic oscillator-like states with a shell spacing ω , which depends on the size of the QD and the depth of the gate potential. We have extended our study to include many-body interactions for systems consisting of up to $N = 6$ holes. The significant spin-orbit splitting in the valence band has led to ground state configurations with spin-down in the $+K$ valley and spin-up in the $-K$ valley, demonstrating the spin-valley locking effect. Our results emphasize the importance of the many-body interactions in controlling the behavior of these systems. Furthermore, for $N = 6$ holes and small QD radii ($R_{QD} < 30$ nm), we have found that the ground states can be accurately determined using around 30 single-particle states. However, for larger QD radii ($R_{QD} > 30$ nm), where the Coulomb interaction becomes stronger, it is necessary to include a larger number of single-particle states to properly establish the ground state. This highlights the sensitivity of the system's behavior to the interplay between confinement and many-body effects.

ACKNOWLEDGMENTS

The authors thank H. Allami, M. Cygorek, J. Manalo, L. Szulakowska, Y. Saleem, M. Mohseni, J. Boddison-Chouinard, A. Bogan, A. Luican-Mayer and L. Gaudreau for valuable discussions.

This work was supported by the Quantum Sensors Challenge Program at the National Research Council of Canada, NSERC QC2DM Strategic Grant No. STPG-521420, NSERC Discovery Grant No. RGPIN-2019-05714, and University of Ottawa Research Chair in Quantum Theory of Materials, Nanostructures, and Devices. M.B. acknowledges financial support from the Polish National Agency for Academic Exchange (NAWA), Poland, grant PPI/APM/2019/1/00085/U/00001. This research was enabled in part by support provided by the Digital Research Alliance of Canada (alliancecan.ca).

-
- [1] A. Splendiani, L. Sun, Y. Zhang, T. Li, J. Kim, C.-Y. Chim, G. Galli, and F. Wang, Emerging photoluminescence in monolayer MoS₂, *Nano letters* **10**, 1271 (2010).
 [2] T. Scrace, Y. Tsai, B. Barman, L. Schweidenback, A. Petrou, G. Kioseoglou, I. Ozfidan, M. Korkusinski,

- and P. Hawrylak, Magnetoluminescence and valley polarized state of a two-dimensional electron gas in WS₂ monolayers, *Nature nanotechnology* **10**, 603 (2015).
 [3] J. G. Roch, G. Froehlicher, N. Leisgang, P. Makk, K. Watanabe, T. Taniguchi, and R. J. Warburton, Spin-

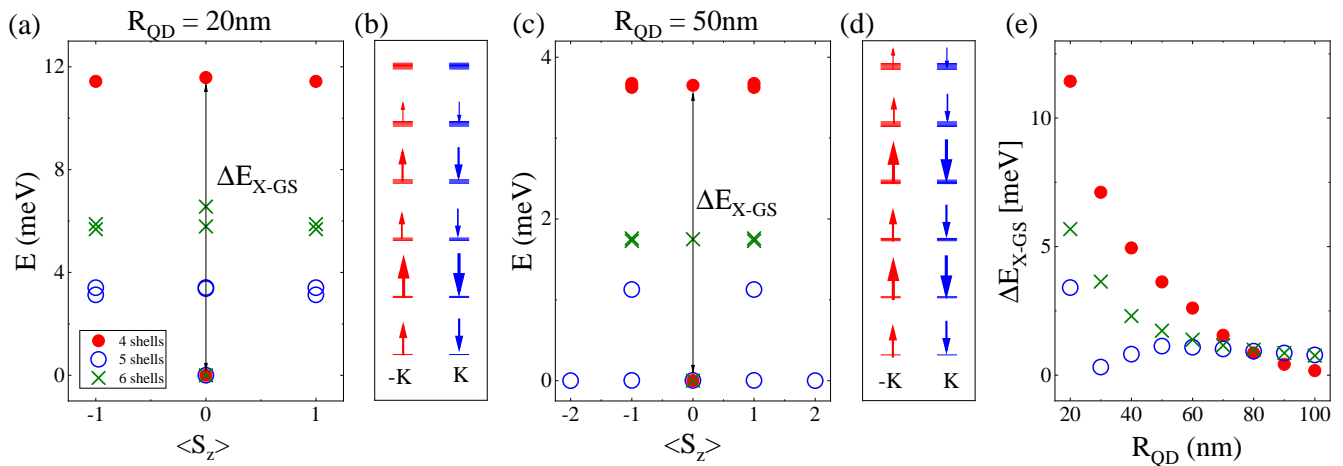


FIG. 6. (Color online) (a) Low-energy spectrum for $N = 6$ holes in a QD with $R_{QD} = 20$ nm. (b), (d) Schematic representation of the ground-state occupation of single-particle QD orbitals. (c) Low-energy spectrum for $N = 6$ holes in a QD with $R_{QD} = 50$ nm. (e) Dependence of the excitation gap on QD size for different numbers of shells included in the many-body calculation. The excitation gap represents the energy separation between the ground state and the first excited states.

- polarized electrons in monolayer MoS₂, *Nature nanotechnology* **14**, 432 (2019).
- [4] D. Van Tuan, A. M. Jones, M. Yang, X. Xu, and H. Dery, Virtual trions in the photoluminescence of monolayer transition-metal dichalcogenides, *Phys. Rev. Lett.* **122**, 217401 (2019).
- [5] H.-P. Komsa and A. V. Krasheninnikov, Two-dimensional transition metal dichalcogenide alloys: stability and electronic properties, *The journal of physical chemistry letters* **3**, 3652 (2012).
- [6] J. Boddison-Chouinard, A. Bogan, N. Fong, K. Watanabe, T. Taniguchi, S. Studenikin, A. Sachrajda, M. Korkusinski, A. Altintas, M. Bieniek, P. Hawrylak, A. Luican-Mayer, and L. Gaudreau, Gate-controlled quantum dots in monolayer WSe₂, *Applied Physics Letters* **119**, 133104 (2021).
- [7] J. Boddison-Chouinard, A. Bogan, P. Barrios, J. Lapointe, K. Watanabe, T. Taniguchi, J. Pawłowski, D. Miravet, M. Bieniek, P. Hawrylak, A. Luican-Mayer, and L. Gaudreau, Anomalous conductance quantization of a one-dimensional channel in monolayer WSe₂, *npj 2D Materials and Applications* **7**, 50 (2023).
- [8] T. Mueller and E. Malic, Exciton physics and device application of two-dimensional transition metal dichalcogenide semiconductors, *npj 2D Materials and Applications* **2**, 1 (2018).
- [9] C. Schneider, M. M. Glazov, T. Korn, S. Höfling, and B. Urbaszek, Two-dimensional semiconductors in the regime of strong light-matter coupling, *Nature communications* **9**, 1 (2018).
- [10] E. S. Kadantsev and P. Hawrylak, Electronic structure of a single MoS₂ monolayer, *Solid state communications* **152**, 909 (2012).
- [11] H. J. Conley, B. Wang, J. I. Ziegler, R. F. Haglund Jr, S. T. Pantelides, and K. I. Bolotin, Bandgap engineering of strained monolayer and bilayer MoS₂, *Nano letters* **13**, 3626 (2013).
- [12] S. Manzeli, D. Ovchinnikov, D. Pasquier, O. V. Yazyev, and A. Kis, 2d transition metal dichalcogenides, *Nature Reviews Materials* **2**, 17033 (2017).
- [13] A. H. Castro Neto, F. Guinea, N. M. R. Peres, K. S. Novoselov, and A. K. Geim, The electronic properties of graphene, *Rev. Mod. Phys.* **81**, 109 (2009).
- [14] K. F. Mak, C. Lee, J. Hone, J. Shan, and T. F. Heinz, Atomically thin MoS₂: A new direct-gap semiconductor, *Phys. Rev. Lett.* **105**, 136805 (2010).
- [15] A. Altıntaş, M. Bieniek, A. Dusko, M. Korkusiński, J. Pawłowski, and P. Hawrylak, Spin-valley qubits in gated quantum dots in a single layer of transition metal dichalcogenides, *Physical Review B* **104**, 195412 (2021).
- [16] M. Bieniek, L. Szulakowska, and P. Hawrylak, Effect of valley, spin, and band nesting on the electronic properties of gated quantum dots in a single layer of transition metal dichalcogenides, *Physical Review B* **101**, 035401 (2020).
- [17] M. Bieniek, M. Korkusiński, L. Szulakowska, P. Potasz, I. Ozfidan, and P. Hawrylak, Band nesting, massive dirac fermions, and valley landé and zeeman effects in transition metal dichalcogenides: A tight-binding model, *Physical Review B* **97**, 085153 (2018).
- [18] Y. Otsuka, S. Yunoki, and S. Sorella, Universal quantum criticality in the metal-insulator transition of two-dimensional interacting dirac electrons, *Phys. Rev. X* **6**, 011029 (2016).
- [19] M. Bieniek, K. Sadecka, L. Szulakowska, and P. Hawrylak, Theory of excitons in atomically thin semiconductors: Tight-binding approach, *Nanomaterials* **12**, 10.3390/nano12091582 (2022).
- [20] F. Wu, F. Qu, and A. H. MacDonald, Exciton band structure of monolayer MoS₂, *Phys. Rev. B* **91**, 075310 (2015).
- [21] H. S. Borges, C. A. N. Júnior, D. S. Brandão, F. Liu, V. V. R. Pereira, S. J. Xie, F. Qu, and A. M. Alcalde, Persistent entanglement of valley exciton qubits in transition metal dichalcogenides integrated into a bimodal optical cavity, *Phys. Rev. B* **107**, 035404 (2023).
- [22] D. Le, A. Barinov, E. Preciado, M. Isarraraz, I. Tanabe, T. Komesu, C. Troha, L. Bartels, T. S. Rahman, and P. A. Dowben, Spin-orbit coupling in the band structure of monolayer WSe₂, *Journal of Physics: Condensed Matter* **27**, 182201 (2015).
- [23] N. Alidoust, G. Bian, S.-Y. Xu, R. Sankar, M. Neupane,

- C. Liu, I. Belopolski, D.-X. Qu, J. D. Denlinger, F.-C. Chou, and M. Z. Hasan, Observation of monolayer valence band spin-orbit effect and induced quantum well states in MoX_2 , *Nature Communications* **5**, 4673 (2014).
- [24] A. D. Güçlü, P. Potasz, M. Korkusinski, and P. Hawrylak, *Graphene quantum dots* (Springer, 2014).
- [25] J. Güttinger, T. Frey, C. Stampfer, T. Ihn, and K. Ensslin, Spin states in graphene quantum dots, *Phys. Rev. Lett.* **105**, 116801 (2010).
- [26] J. A. McGuire, Growth and optical properties of colloidal graphene quantum dots, *Physica Status Solidi* **10**, 91 (2016).
- [27] S. Wang, N. Khariche, E. Costa Girão, X. Feng, K. Müllen, V. Meunier, R. Fasel, and P. Ruffieux, Quantum dots in graphene nanoribbons, *Nano Letters* **17**, 4277 (2017).
- [28] K. Wang, K. De Greve, L. A. Jauregui, A. Sushko, A. High, Y. Zhou, G. Scuri, T. Taniguchi, K. Watanabe, M. D. Lukin, H. Park, and P. Kim, Electrical control of charged carriers and excitons in atomically thin materials, *Nature Nanotechnology* **13**, 128 (2018).
- [29] R. Pisoni, Z. Lei, P. Back, M. Eich, H. Overweg, Y. Lee, K. Watanabe, T. Taniguchi, T. Ihn, and K. Ensslin, Gate-tunable quantum dot in a high quality single layer MoS_2 van der Waals heterostructure, *Applied Physics Letters* **112**, 123101 (2018).
- [30] C. Volk, S. Fringes, B. Terrés, J. Dauber, S. Engels, S. Trellenkamp, and C. Stampfer, Electronic excited states in bilayer graphene double quantum dots, *Nano Letters* **11**, 3581 (2011).
- [31] M. T. Allen, J. Martin, and A. Yacoby, Gate-defined quantum confinement in suspended bilayer graphene, *Nature Communications* **3**, 934 (2012).
- [32] M. Eich, F. c. v. Herman, R. Pisoni, H. Overweg, A. Kurzmann, Y. Lee, P. Rickhaus, K. Watanabe, T. Taniguchi, M. Sigrist, T. Ihn, and K. Ensslin, Spin and valley states in gate-defined bilayer graphene quantum dots, *Phys. Rev. X* **8**, 031023 (2018).
- [33] A. Kurzmann, M. Eich, H. Overweg, M. Mangold, F. Herman, P. Rickhaus, R. Pisoni, Y. Lee, R. Garreis, C. Tong, K. Watanabe, T. Taniguchi, K. Ensslin, and T. Ihn, Excited states in bilayer graphene quantum dots, *Phys. Rev. Lett.* **123**, 026803 (2019).
- [34] N. M. Freitag, L. A. Chizhova, P. Nemes-Incze, C. R. Woods, R. V. Gorbachev, Y. Cao, A. K. Geim, K. S. Novoselov, J. Burgdörfer, F. Libisch, and M. Morgenstern, Electrostatically confined monolayer graphene quantum dots with orbital and valley splittings, *Nano Letters* **16**, 5798 (2016).
- [35] Y. Saleem, K. Sadecka, M. Korkusinski, D. Miravet, A. Dusko, and P. Hawrylak, Theory of excitons in gated bilayer graphene quantum dots, *Nano Letters* **23**, 2998 (2023).
- [36] M. Brotons-Gisbert, A. Branny, S. Kumar, R. Picard, R. Proux, M. Gray, K. S. Burch, K. Watanabe, T. Taniguchi, and B. D. Gerardot, Coulomb blockade in an atomically thin quantum dot coupled to a tunable Fermi reservoir, *Nature Nanotechnology* **14**, 442 (2019).
- [37] X. Lu, X. Chen, S. Dubey, Q. Yao, W. Li, X. Wang, Q. Xiong, and A. Srivastava, Optical initialization of a single spin-valley in charged WSe_2 quantum dots, *Nature Nanotechnology* **14**, 426 (2019).
- [38] C. Chakraborty, L. Qiu, K. Konthasinghe, A. Mukherjee, S. Dhara, and N. Vamivakas, 3D Localized Trions in Monolayer WSe_2 in a Charge Tunable van der Waals Heterostructure, *Nano Letters* **18**, 2859 (2018).
- [39] Z.-Z. Zhang, X.-X. Song, G. Luo, G.-W. Deng, V. Mosallanejad, T. Taniguchi, K. Watanabe, H.-O. Li, G. Cao, G.-C. Guo, F. Nori, and G.-P. Guo, Electrotunable artificial molecules based on van der Waals heterostructures, *Science Advances* **3**, e1701699 (2017).
- [40] S. Bhandari, K. Wang, K. Watanabe, T. Taniguchi, P. Kim, and R. Westervelt, Imaging quantum dot formation in MoS_2 nanostructures, *Nanotechnology* **29**, 42LT03 (2018).
- [41] Q. Chen, L. Li, and F. Peeters, Magnetic field dependence of electronic properties of MoS_2 quantum dots with different edges, *Physical Review B* **97**, 085437 (2018).
- [42] L. Szulakowska, M. Cygorek, M. Bieniek, and P. Hawrylak, Valley- and spin-polarized broken-symmetry states of interacting electrons in gated MoS_2 quantum dots, *Phys. Rev. B* **102**, 245410 (2020).
- [43] J. Pawłowski, M. Bieniek, and T. Woźniak, Valley two-qubit system in a MoS_2 -monolayer gated double quantum dot, *Phys. Rev. Appl.* **15**, 054025 (2021).
- [44] X.-X. Song, D. Liu, V. Mosallanejad, J. You, T.-Y. Han, D.-T. Chen, H.-O. Li, G. Cao, M. Xiao, G.-C. Guo, and G.-P. Guo, A gate defined quantum dot on the two-dimensional transition metal dichalcogenide semiconductor WSe_2 , *Nanoscale* **7**, 16867 (2015).
- [45] S. Raymond, S. Studenikin, A. Sachrajda, Z. Wasilewski, S. J. Cheng, W. Sheng, P. Hawrylak, A. Babinski, M. Potemski, G. Ortner, and M. Bayer, Excitonic energy shell structure of self-assembled InGaAs/GaAs quantum dots, *Phys. Rev. Lett.* **92**, 187402 (2004).
- [46] J. Zhou, W.-Y. Shan, W. Yao, and D. Xiao, Berry phase modification to the energy spectrum of excitons, *Phys. Rev. Lett.* **115**, 166803 (2015).
- [47] A. Srivastava and A. Imamoğlu, Signatures of Bloch-band geometry on excitons: Nonhydrogenic spectra in transition-metal dichalcogenides, *Phys. Rev. Lett.* **115**, 166802 (2015).
- [48] L. Keldysh, Coulomb interaction in thin semiconductor and semimetal films, *Sov. J. Exp. Theor. Phys. Lett.* **29**, 658 (1979).
- [49] M. Korkusinski, W. Sheng, and P. Hawrylak, Designing quantum systems in self-assembled quantum dots, *Physica Status Solidi (b)* **238**, 246 (2003).
- [50] S. R. White, Density matrix formulation for quantum renormalization groups, *Phys. Rev. Lett.* **69**, 2863 (1992).
- [51] U. Schollwöck, The density-matrix renormalization group, *Rev. Mod. Phys.* **77**, 259 (2005).